Preliminary qualification of a machine learning-based assessment of the tumour immune infiltrate as a predictor of outcome in patients with hepatocellular carcinoma treated with atezolizumab plus bevacizumab – Supplementary Material

Bernhard Scheiner[1,2], Pasquale Lombardi[1,3], Antonio D´Alessio[1], Gwangil Kim[4], Masoud Tafavvoghi[5], Oleksandr Petrenko[2,6], Robert D. Goldin[1], Claudia A.M. Fulgenzi[1], Aria Torkpour[1], Lorenz Balcar[2], Francesco A. Mauri[1], Katharina Pomej[2], Vera Himmelsbach[7], Maryam Barsch[8], Ciro Celsa[9], Giuseppe Cabibbo[9], Jaekyung Cheon[10], Anja Krall[11], Florian Hucke[12], Luca Di Tommaso[13,14], Monica Bernasconi[13], Lorenza Rimassa[13,15], Adel Samson[16], Bernardo Stefanini[17], Behrang Mozayani[18], Michael Trauner[2], Carolin Lackner[19], Rudolf Stauber[11], Francesco Vasuri[20], Fabio Piscaglia[17,21], Bertram Bengsch[8], Fabian Finkelmeier[7], Markus Peck-Radosavljevic[12], Lill-Tove Rasmussen Busund[22], Teresa Marafioti[23], Mohammad Rahbari[24], Mathias Heikenwälder[24], Matthias Pinter[2], Hong Jae Chon[10§], Mehrdad Rakaee[5,22*], David J. Pinato[1,25*,§]

*equally contributing senior authors

[§]corresponding authors

Affiliations:

1. Department of Surgery & Cancer, Imperial College London, United Kingdom
2. Division of Gastroenterology and Hepatology, Department of Internal Medicine III, Medical University of Vienna, Austria
3. Phase 1 Unit, Fondazione Policlinico Universitario A. Gemelli, IRCCS, Università Cattolica del Sacro Cuore, Rome, Italy
4. Department of Pathology, CHA Bundang Medical Center, CHA University, Seongnam, Republic of Korea
5. Department of Cancer Genetics, Oslo University Hospital, Oslo, Norway.
6. Ukrainian Institute for Systems Biology and Medicine, 04119 Kyiv, Ukraine
7. Department of Gastroenterology and Hepatology, University Hospital Frankfurt, Frankfurt, Germany
8. Department of Internal Medicine II, Medical Center - University of Freiburg, Freiburg, Germany
9. Gastroenterology and Hepatology Unit, Department of Health Promotion, Mother & Child Care, Internal Medicine & Medical Specialties, University of Palermo, Palermo, Italy
10. Medical Oncology, Department of Internal Medicine, CHA Bundang Medical Center, CHA University School of Medicine, Seongnam, Korea.

11. Department of Internal Medicine, Division of Gastroenterology and Hepatology, Medical University of Graz, Austria
12. Internal Medicine and Gastroenterology (IMuG), Including Centralized Emergency Service (ZAE), Klinikum Klagenfurt am Wörthersee, Klagenfurt, Austria.
13. Department of Biomedical Sciences, Humanitas University, Pieve Emanuele, Milan, Italy
14. Pathology Department, IRCCS Humanitas Research Hospital, Rozzano, Milan, Italy.
15. Medical Oncology and Hematology Unit, Humanitas Cancer Center, IRCCS Humanitas Research Hospital, Rozzano, Milan, Italy
16. Leeds Institute of Medical Research at St James's (LIMR), School of Medicine, Faculty of Medicine and Health, University of Leeds, St James's University Hospital, Leeds, UK.
17. Department of Medical and Surgical Sciences, Bologna University, 40138 Bologna, Italy.
18. Department of Pathology, Medical University of Vienna, Vienna, Austria
19. Diagnostic and Research Institute of Pathology, Medical University of Graz, Austria
20. Pathology Unit, IRCCS - Azienda Ospedaliero-Universitaria di Bologna, 40138, Bologna, Italy
21. Division of Internal Medicine, Hepatobiliary and Immunoallergic Diseases, IRCCS Azienda Ospedaliero-Universitaria di Bologna, 40138 Bologna, Italy.
22. Department of Clinical Pathology, University Hospital of North Norway, Tromso, Norway.
23. Department of Histopathology, University College London Hospital, London, UK.
24. Division of Chronic Inflammation and Cancer, German Cancer Research Center (DKFZ), Heidelberg, Germany
25. Department of Translational Medicine, University of Piemonte Orientale, Novara, Italy

Corresponding authors:

Prof. Dr. Hong Jae Chon, MD
Medical Oncology, Department of Internal Medicine
CHA Bundang Medical Center, CHA University,
Seongnam 13496, Korea.
minidoctor@cha.ac.kr

Prof. Dr. Mehrdad Rakaee, MD PhD
Department of Cancer Genetics
Institute for Cancer Research
Oslo University Hospital
0379 Oslo, Norway
mehrdad.rakaee@uit.no

Dr. David J. Pinato, MD PhD
Imperial College London Hammersmith Campus,
Du Cane Road, W12 0HS, London, UK.
david.pinato@imperial.ac.uk

Table of contents

Supplementary Methods

A+B cohort

The *A+B cohort* included 102 patients. In line with IMbrave150 inclusion criteria [1], patients were required to have well-preserved liver function (Child-Pugh class A cirrhosis) and an ECOG performance status of 0-2 at treatment initiation. Patient and tumour characteristics including demographic data, data on previous surgical or loco-regional treatments, the tumour stage and important laboratory values at baseline as well as key clinical outcomes (overall and progression-free survival as well as radiological response as evaluated by the local investigators according to RECIST 1.1) were retrospectively assessed from clinical records.

mIHC cohort

The multiplexed immunohistochemistry cohort (*mIHC cohort*) included 62 patients, in whom tissue slides from resection specimen were collected. Baseline tumour and patient characteristics were extracted from clinical documentation systems. Next to H&E staining, multiplex immunostainings (mIHC) for CD4+, CD4+FOXP3+, CD8+, and CD8+PD1+ T-cells were performed on 5 µm tissue sections as previously described [2]. Following staining, tissue microphotographs were manually assessed at 40x magnification to derive the density of each cell type per mm^2 of tissue. Cellular density was scored as the mean of three independent readings deriving separate values for tumoural, peri-tumoural and non-tumoural areas as available on the individual slides. As the automatic ICI quantification was performed on whole slides including all areas, the mean of the evaluable areas on the mIHC slides was calculated.

RNAseq cohort

The *RNAseq cohort* included 44 patients who underwent curative resection for HCC. In these patients routine H&E stained slides were digitized and bulk RNA sequencing was performed.

After RNA extraction, reverse transcription into cDNA and amplification, sequencing was performed using next-generation sequencing (NGS) technology as previously described [3].

Machine-learning approach for ICI identification and quantification

The supervised machine learning (ML) algorithm was developed using QuPath (v.0.4.2) and followed the previously described procedure with some modifications [4, 5]. In summary, the first step included color deconvolution to estimate the stain vectors and to normalize the RGB channels per slide. Next, the Stardist DeepLearning extension (https://qupath.readthedocs.io/en/0.4/docs/deep/stardist.html) using a convolutional neural network was used to detect cells based on different properties of nuclei [5, 6]. We used the publicly available model file “he_heavy_augment.pb”, without retraining or fine-tuning, and with a prediction threshold set at 0.3. Preprocessing included subtracting a baseline value of 100 and normalizing by division by 100 to adjust for intensity variations. The detection was performed at a resolution of 0.5 µm/pixel and the model included prediction probability as an additional measurement for each detection. Threshold tuning was guided by expert pathologist review across multiple ROIs and slides. Afterwards, an object-based classifier was trained using annotation-guided random decision forest cell classifiers guided by expert pathologists (L.T.B) to retain immune, tumor and stroma cells (Supplementary Figure 1). ICIs were defined as mononuclear immune cells, including lymphocytes and plasma cells. The training dataset was constructed by randomly selecting regions of interest (ROIs) of 0.25 mm^2 from approximately 50% of slides in the training cohort. ROIs were selected across various tissue compartments (tumor epithelium, stroma, and immune-rich areas), and were stitched together into a composite training image. Cell annotations were performed by an experienced pathologist, with ~2000 point annotations across three major classes: tumor, ICI, and stromal cells. Care was taken to maintain class balance during annotation. The classifier was trained using QuPath’s built-in random forest algorithm with the following parameters: max_depth = 25, min_samples = 5, max_trees = 100, and active_vars = 10. Features used for nuclei characterization included RGB values, hematoxylin and eosin stain intensities, multiscale sigma features (σ = 1, 2, 4, 8), and texture-based descriptors such as

Laplacian, gradient magnitude, and weighted deviation, derived from difference of Gaussian filters. The source code as well as a step-by-step guide demonstrating how to apply the method within the QuPath graphical user interface is publicly available on github with the following link: https://github.com/TMasoud/Machine-learning-based-assessment-of-the-tumour-immune-infiltrate.

Finally, the *RNA seq and mIHC* cohorts served as independent technical controls.

Statistics

Baseline patient and tumour characteristics were summarized using descriptive statistics. Categorical variables were reported as absolute and relative frequencies, whereas continuous variables were shown as mean ± standard deviation (SD) or median (interquartile range [IQR]), as applicable. Student's t-test was used for group comparisons of normally distributed variables, while the Mann-Whitney-U-test was applied for non-normally distributed variables. Group comparisons of categorical variables were performed using either Chi-squared or Fisher's exact test.

Overall survival (OS) was defined as the time from A+B initiation until death, and patients who were still alive or lost to follow-up at the time of data collection were censored at the date of last contact. PFS was defined as the time to radiological progression or death. Patients who were still alive or lost to follow-up without radiological progression were censored at the date of last contact. Time on treatment was defined as the time from treatment start until end of treatment and patients who were alive or lost to follow-up with ongoing treatment were censored at the date of last contact. Median overall survival/PFS/time on treatment were calculated by the Kaplan-Meier method, while median estimated follow-up was calculated using the reverse Kaplan-Meier method [7]. All outcomes in the A+B as well as the mIHC cohort were assessed comparing the ICI-high vs. ICI-low cohorts as derived from the optimal cut-point calculation. The functional form of the effects of continuous ICI counts on OS was flexibly assessed with restricted cubic splines [8].

The level of significance was set at a 2-sided p-value < 0.05.

Analysis of RNA sequencing data

The following analysis has been performed in GNU R (v.4.3.3). Mapped gene counts were annotated using biomaRt (v.2.56.1) [9], and only protein-coding genes were used in the following analysis. Given the significantly lower density of the ICI in the RNAseq cohort as compared to the other cohorts and in order to detect differences in gene expression profiles, the patient population was split by ICI tertiles and patients with TIL counts below the first (ICI-low) and above the third tertile (ICI-high) were compared. Differential expression testing between ICI-high and ICI-low groups was performed with DESeq2 with Wald test (v.1.40.2) [10], the fold-change inflation was adjusted with ashr (v.2.2-63) [11], and multiple testing adjustment has been performed with independent hypothesis weighting with Benjamini Hochberg adjustment using group factor as a covariate (IHW, v.1.28.0) [12]. $P_{adjusted}$ of ≤ 0.05 and log_2FC > |0.5| were used to identify significantly dysregulated genes. The exploration has been performed using PCAtools (v.2.12.0, REF: Blighe, K, and A Lun. 2019. “PCAtools: everything Principal Components Analysis.” https://github.com/kevinblighe/PCAtools). Visualization of the differentially expressed genes has been done with EnhancedVolcano (v.1.20.0, REF: Blighe, K, S Rana, and M Lewis. 2018. “EnhancedVolcano: Publication-ready volcano plots with enhanced colouring and labeling.” https://github.com/kevinblighe/EnhancedVolcano). The components showing the best group separation (namely, component #1 and #3) were used for the following analysis. Immune gene signatures were calculated using MCP-counter method (https://genomebiology.biomedcentral.com/articles/10.1186/s13059-016-1070-5).

Co-expressed gene modules were detected using CEMiTool (v.1.24.0) [13] on rlog-normalized counts. Then, eigengenes of the obtained modules were extracted and were correlated to clinical metadata using Spearman correlation. Genes of the modules with P-value < 0.05 and correlation coefficient > |0.6| for ICI were extracted for functional analysis.

For functional analysis, gProfiler2 (v.0.2.3) [14], and clusterProfiler (v.4.8.1) [15] were used. In the context without gene ranking (i.e., genes of principal components and co-expressing

gene modules), gProfiler2 was used for over-representation testing against the following gene set databases, latest editions: Gene Ontology: Molecular Function; Reactome; WikiPathways; KEGG. For gene set enrichment analysis, clusterProfiler was used on the gene output of DESeq2 using the following ranking approach: sign(log2(Fold Change)) * (-log10(Padjusted) against MSigDB Hallmark Pathways (v.2023).

Supplementary Results

ML cell classification interpretability

For ML-based cell classification, interpretability was assessed through feature importance analysis. The most discriminative factors were morphometric descriptors, particularly the Nucleus/Cell area ratio at both 25 µm and 50 µm scales. Haralick texture features from brightness and color channels also ranked highly, capturing chromatin texture and nuclear heterogeneity (**Supplementary Figure S6**).

Correlations between ICI scores and RNA-seq based immune signatures

Additionally, the ML-derived ICI scores showed a significant moderate correlation with RNA-seq–based immune signatures for T cells (r = 0.37) and B cells (r = 0.34), supporting the model's ability to identify mononuclear immune cell infiltration (**Supplementary Figure S7)**.

Differences in cell populations between patients with ICI-high vs. ICI-low

Tumour and stroma cell density was significantly different between ICI-high and ICI-low patients (tumour cell density: ICI-high: 3295.9, IQR: 2016.0-4253.5 vs. ICI-low: 3935.2, IQR: 2536.1-4906.4 cells/mm^2; p=0.043 and stroma cell density: ICI-high: 1360.7, IQR: 591.9-2055.9 vs. ICI-low: 192.1, IQR: 61.9-510.8 cells/mm^2; p<0.001).

Transcriptomic features of ICI-high patients

The functional gene set analysis showed that ICI-high had significantly upregulated pathways associated with inflammation (e.g. those described in allograft rejection, inflammatory response, TNFα-signalling via NFκB, interferon-γ, etc.), while pathways associated with metabolite metabolism (e.g. fatty acid metabolism, bile acid metabolism, etc.) were downregulated (**Figure 2B**). Furthermore, we detected 1507 differentially expressed genes under the established thresholds (**Figure 2C**). Matrix remodelling genes were among the most upregulated in ICI-high (namely: COL6A3, MMP2, MMP11, ADAMTS15, COL1A1, FNDC1). Furthermore, IL7R, CXCR4, ITAX, and CTLA4 were significantly upregulated, hinting at more pronounced processes involved in infiltrate formation and immune cell

crosstalk. In turn, we observed a downregulation of several solute carriers (SLC13A3, SLC22A12, SLC12A1) and enzymes (GLUL, ACSM1), suggesting further disruptions in ion turnover and lipid metabolism with more dense immune cell infiltration. The most downregulated gene was HHIPL2, which role was not previously described in the context of HCC, and evidence suggesting its modulation by iron concentration in the microenvironment [16] (**Supplementary Data 1**). Despite suboptimal separation based on the main principal components (PC, **Figure 2C**), the combination of PC1 and PC3 separated the groups, explaining together 25.22% of transcriptomic variance in the cohort dataset (**Supplementary Figure 8A and 8B**). Genes of PC1 were mostly enriched in gene sets related to matrix organization, cytochrome function, and nuclear receptors, while PC3 consisted of sets related to small molecule turnover, xenobiotic metabolism, retinol, and NRF2 pathways (**Supplementary Figures 8C and 8D**).

The gene set analysis focused on biological processes (GO:BP) identified upregulated T-cell and pro-inflammatory signatures in ICI-high, including IL-2 signalling, while mitochondrial respiration was suppressed (**Supplementary Figure 9A and 9B**). Upon further investigation of respiration-related pathways, we found peroxisome proliferator-activated receptor α (PPARα) downregulation in ICI-high (**Supplementary Figure 9C**). Its suppression in HCC has previously been associated with a hindered ability to regulate the release of neutrophil extracellular traps, thus contributing to inflammation in the microenvironment [17]. The complete network of dysregulated gene sets in ICI-high is presented in **Supplementary Figure 10**.

Finally, we performed gene co-expression analysis and linked modules of highly co-expressed genes to patient metadata (**Supplementary Figure 11**). Specifically, gene module M4, consisting of 101 genes, had a strong positive association with quantified stroma percentage and ICI abundance (**Supplementary Figure 11A, Supplementary Data 2**). The most significant genes of this module showed different regulation directions between ICI-high and ICI-low (**Supplementary Figure 11B**), with STC1 and EPS8L3 showing the highest

enrichment in the ICI-low group. Overall, the module genes were linked to metal turnover, cytochromes functions, retinol, and fatty acid metabolism (**Supplementary Figure 11C**).

REFERENCES

[1] Finn RS, Qin S, Ikeda M, Galle PR, Ducreux M, Kim TY, et al. Atezolizumab plus Bevacizumab in Unresectable Hepatocellular Carcinoma. N Engl J Med 2020;382:1894-1905.

[2] Pinato DJ, Murray SM, Forner A, Kaneko T, Fessas P, Toniutto P, et al. Trans-arterial chemoembolization as a loco-regional inducer of immunogenic cell death in hepatocellular carcinoma: implications for immunotherapy. J Immunother Cancer 2021;9.

[3] Pfister D, Nunez NG, Pinyol R, Govaere O, Pinter M, Szydlowska M, et al. NASH limits anti-tumour surveillance in immunotherapy-treated HCC. Nature 2021;592:450-456.

[4] Rakaee M, Adib E, Ricciuti B, Sholl LM, Shi W, Alessi JV, et al. Association of Machine Learning-Based Assessment of Tumor-Infiltrating Lymphocytes on Standard Histologic Images With Outcomes of Immunotherapy in Patients With NSCLC. JAMA Oncol 2022.

[5] Bankhead P, Loughrey MB, Fernandez JA, Dombrowski Y, McArt DG, Dunne PD, et al. QuPath: Open source software for digital pathology image analysis. Sci Rep 2017;7:16878.

[6] Schmidt U, Weigert M, Broaddus C, Myers G. Cell Detection with Star-Convex Polygons. In: Frangi AF, Schnabel JA, Davatzikos C, Alberola-López C, Fichtinger G, editors. Medical Image Computing and Computer Assisted Intervention – MICCAI 2018; 2018 2018//; Cham: Springer International Publishing; 2018. p. 265-273.

[7] Schemper M, Smith TL. A note on quantifying follow-up in studies of failure time. Control Clin Trials 1996;17:343-346.

[8] Heinzl H, Kaider A. Gaining more flexibility in Cox proportional hazards regression models with cubic spline functions. Comput Methods Programs Biomed 1997;54:201-208.

[9] Smedley D, Haider S, Ballester B, Holland R, London D, Thorisson G, et al. BioMart – biological queries made easy. BMC Genomics 2009;10:22.

[10] Love MI, Huber W, Anders S. Moderated estimation of fold change and dispersion for RNA-seq data with DESeq2. Genome Biology 2014;15:550.

[11] Stephens M. False discovery rates: a new deal. Biostatistics 2016;18:275-294.

[12] Ignatiadis N, Klaus B, Zaugg JB, Huber W. Data-driven hypothesis weighting increases detection power in genome-scale multiple testing. Nature Methods 2016;13:577-580.

[13] Russo PST, Ferreira GR, Cardozo LE, Bürger MC, Arias-Carrasco R, Maruyama SR, et al. CEMiTool: a Bioconductor package for performing comprehensive modular co-expression analyses. BMC Bioinformatics 2018;19:56.

[14] Kolberg L, Raudvere U, Kuzmin I, Vilo J, Peterson H. gprofiler2 -- an R package for gene list functional enrichment analysis and namespace conversion toolset g:Profiler. F1000Res 2020;9.

[15] Yu G, Wang L-G, Han Y, He Q-Y. clusterProfiler: an R Package for Comparing Biological Themes Among Gene Clusters. OMICS: A Journal of Integrative Biology 2012;16:284-287.

[16] Doyard M, Fatih N, Monnier A, Island ML, Aubry M, Leroyer P, et al. Iron excess limits HHIPL-2 gene expression and decreases osteoblastic activity in human MG-63 cells. Osteoporos Int 2012;23:2435-2445.

[17] Pan B, Zhang Z, Ye D, Zhang X, Yao Y, Luo Y, et al. PPARα suppresses growth of hepatocellular carcinoma in a high-fat diet context by reducing neutrophil extracellular traps release. JHEP Reports 2024:101228.

Supplementary Tables

Supplementary Table 1 Patient characteristics of the *mIHC* and the *RNAseq cohorts*

	***mIHC cohort* (n=62)**	***RNAseq cohort* (n=44)**
Sex		
Male, n (%)	46 (79.3%)	37 (84.1%)
Cirrhosis, n (%)	55 (90.2%)	30 (68.2%)
Etiology of liver disease		
HBV, n (%)	7 (12.3%)	10 (22.7%)
HCV, n (%)	47 (78.3%)	-
Alcohol, n (%)	9 (16.1%)	20 (45.5%)
NAFLD/NASH, n (%)	2 (15.2%)	16 (36.4%)
Other, n (%)	3 (15.4%)	-
Child-Pugh-Class*		
Child-Pugh Class A, n (%)	48 (82.8%)	34 (77.3%)
Child-Pugh Class B, n (%)	9 (15.5%)	3 (6.8%)
Child-Pugh Class C, n (%)	1 (1.7%)	-
BCLC stage		
0, n (%)	-	2 (4.5%)
A, n (%)	53 (85.5%)	17 (38.6%)
B, n (%)	9 (14.5%)	25 (56.8%)
AFP (ng/mL), median (IQR)**	21.6 (6.1-120.1)	7 (5-73)
ICI cells/mm^2	432.2 (284.2-596.3)	205 (96-373)
CD4+ cells, average cells/mm^2	366.2 (231.5-566.4)	-
CD4+FOXP3+ cells, average cells/mm^2	33.4 (10.9-61.5)	-
CD8+ cells, average cells/mm^2	296.8 (210.0-462.9)	-
CD8+PD1+ cells, average cells/mm^2	50.6 (13.6-84.4)	-

Abbreviations: AFP, alpha-fetoprotein; BCLC, Barcelona-Clinic Liver Cancer; ECOG PS, Eastern Cooperative Oncology Group Performance Status; ICI, immune cell infiltrate cells/mm^2

* Child-Pugh classification was not available in 7 patients in the *RNAseq* cohort

** AFP levels were not available in 12 patients in the *RNAseq* cohort

Supplementary Figures

Supplementary Figure 1

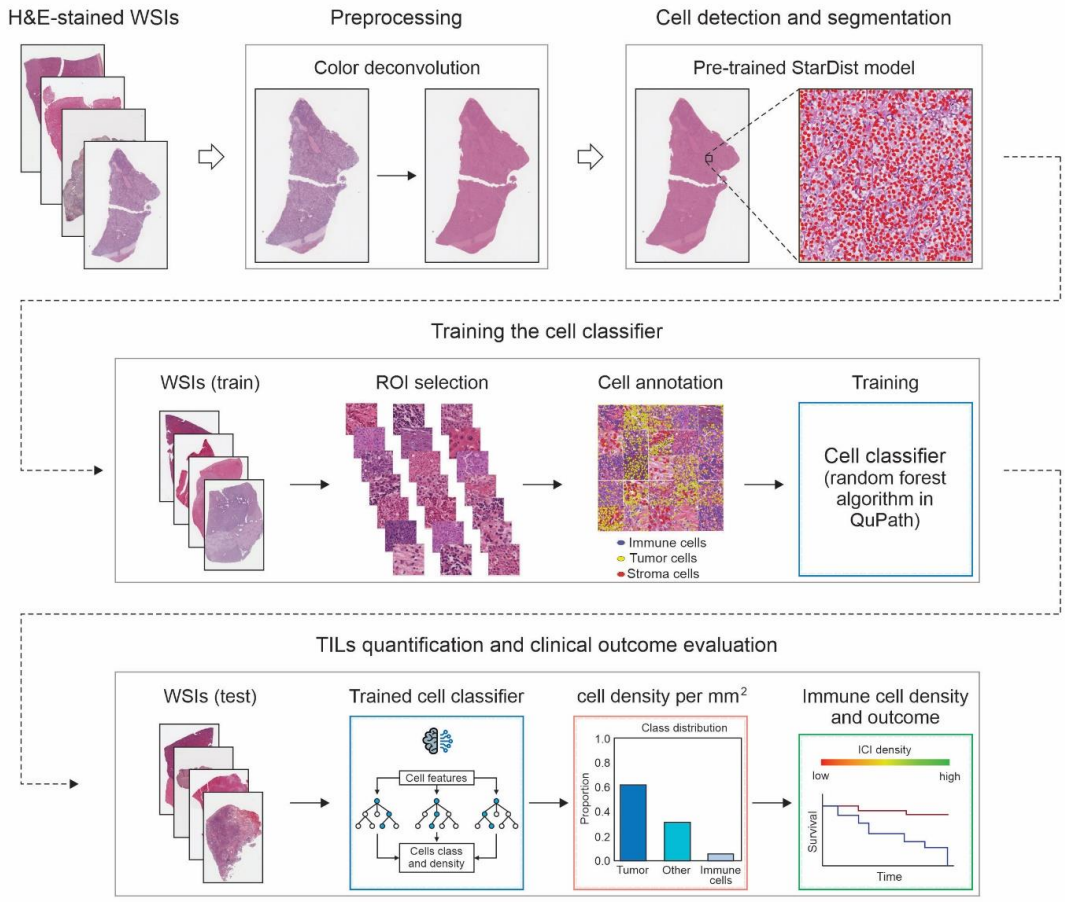

Supplementary Figure 1 Schematic overview of the machine learning methods used in this manuscript

Supplementary Figure 2

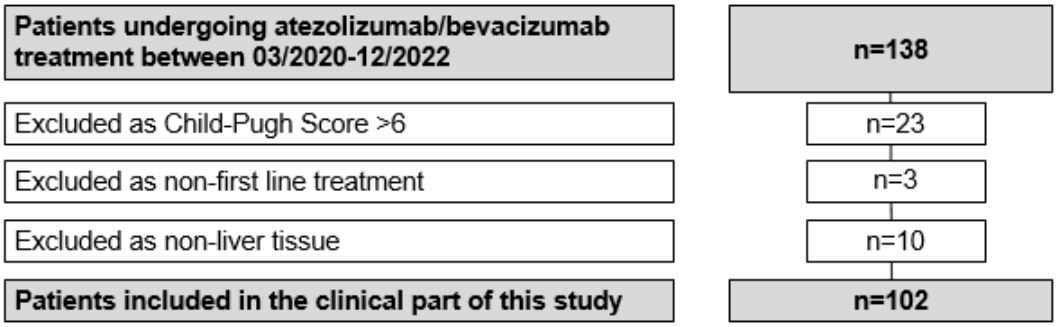

Supplementary Figure 2 Patient flowchart demonstrating in- and exclusion criteria for patients considered for the *A+B cohort*

Supplementary Figure 3

3A

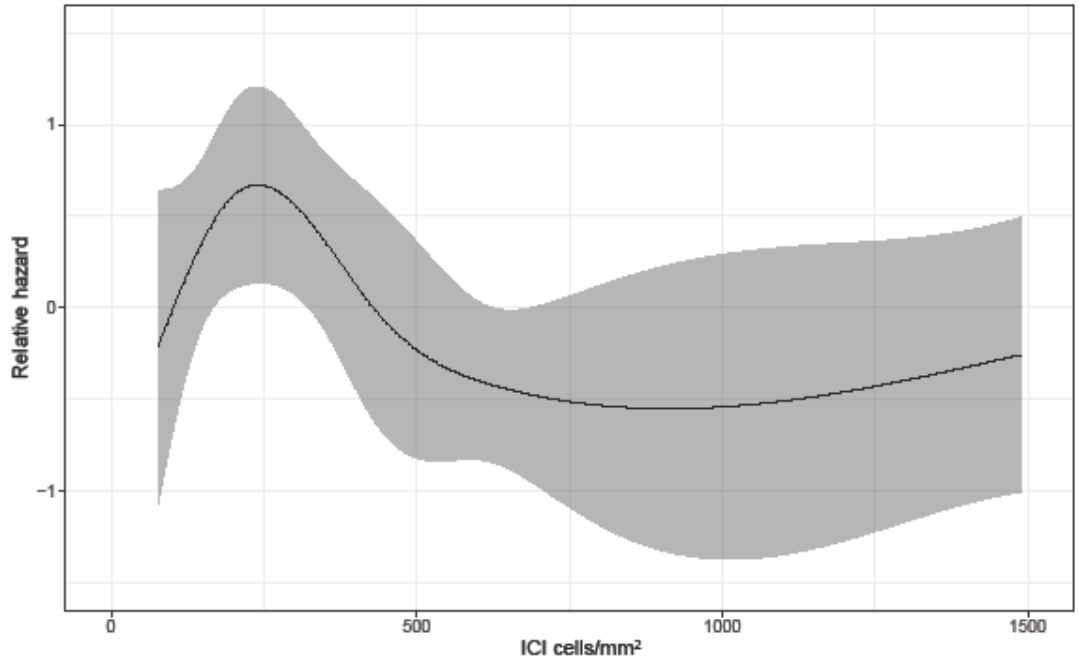

3B

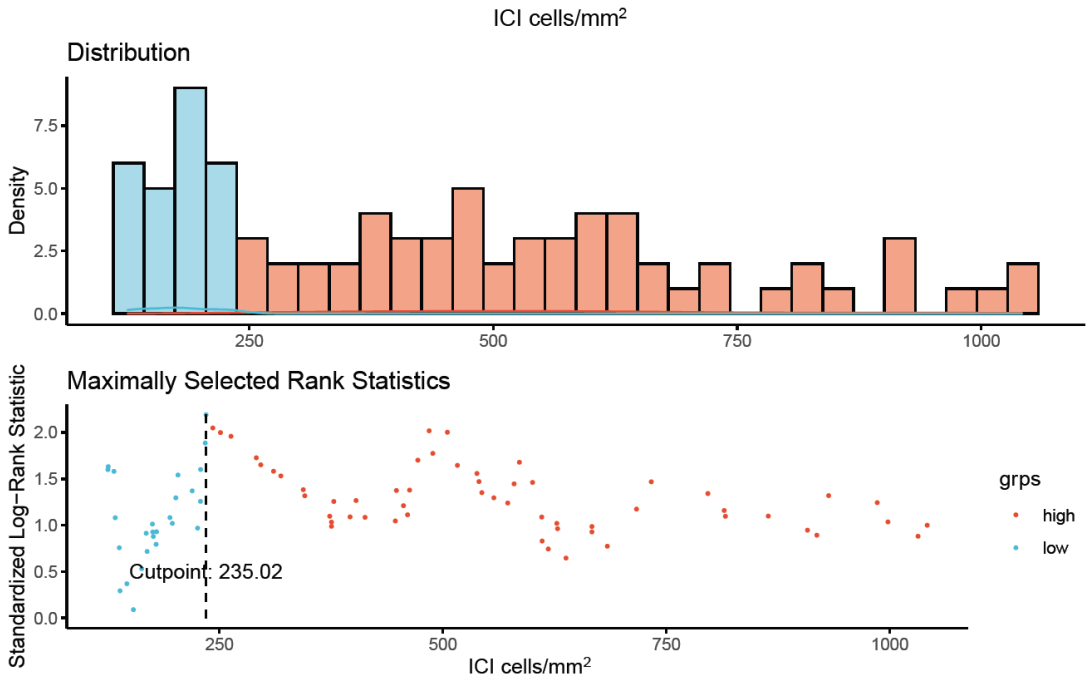

Supplementary Figure 3A Restricted cubic spline analyses for ICI cells/mm^2. Log hazard ratio function and 95 % pointwise confidence band estimated by a restricted cubic spline function for quantifying the effect of the ICI on overall survival. Smaller log hazard ratios indicate better survival. **3B** Immune cell infiltrate (ICI, cells/mm^2) cut-point identification for overall survival (OS) based on maximally selected rank-statistics.

Abbreviations: ICI, immune cell infiltrate

Supplementary Figure 4.

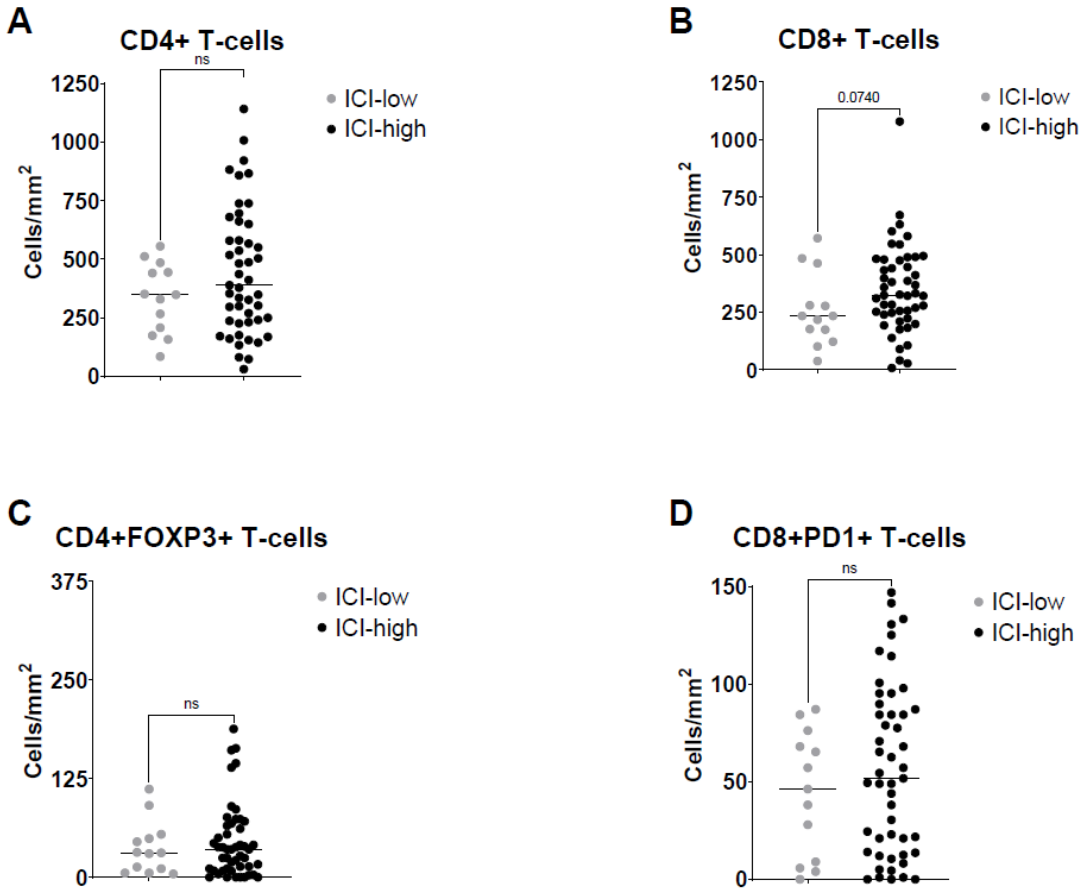

Supplementary Figure 4. Comparison of **A** CD4+ T-cell, **B** CD8+ T-cell, **C** CD4+FOXP3+ T-cell and **D** CD+PD1+ T-cell counts/mm^2 between patients with ICI-high vs. ICI-low.

Supplementary Figure 5.

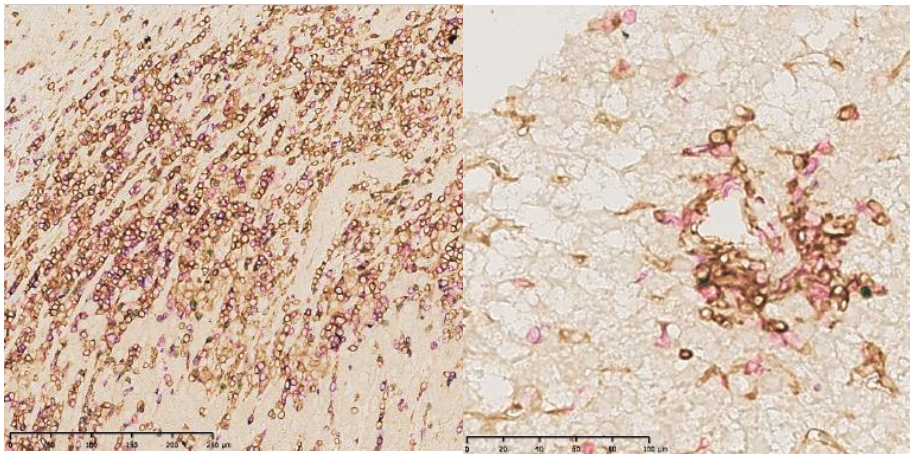

Supplementary Figure 5. Representative multiplex immunohistochemistry (mIHC) images of hepatocellular carcinoma tissue at two different magnifications. Staining pattern: CD4+ T cells (brown, cell surface), CD8+ T cells (red, cell surface), CD4+FOXP3+ regulatory T cells (brown surface with green nucleus), PD-1+ cells (blue, cell surface). CD8+PD-1+ double-positive cells appear violet due to co-localization of red and blue staining.

Supplementary Figure 6.

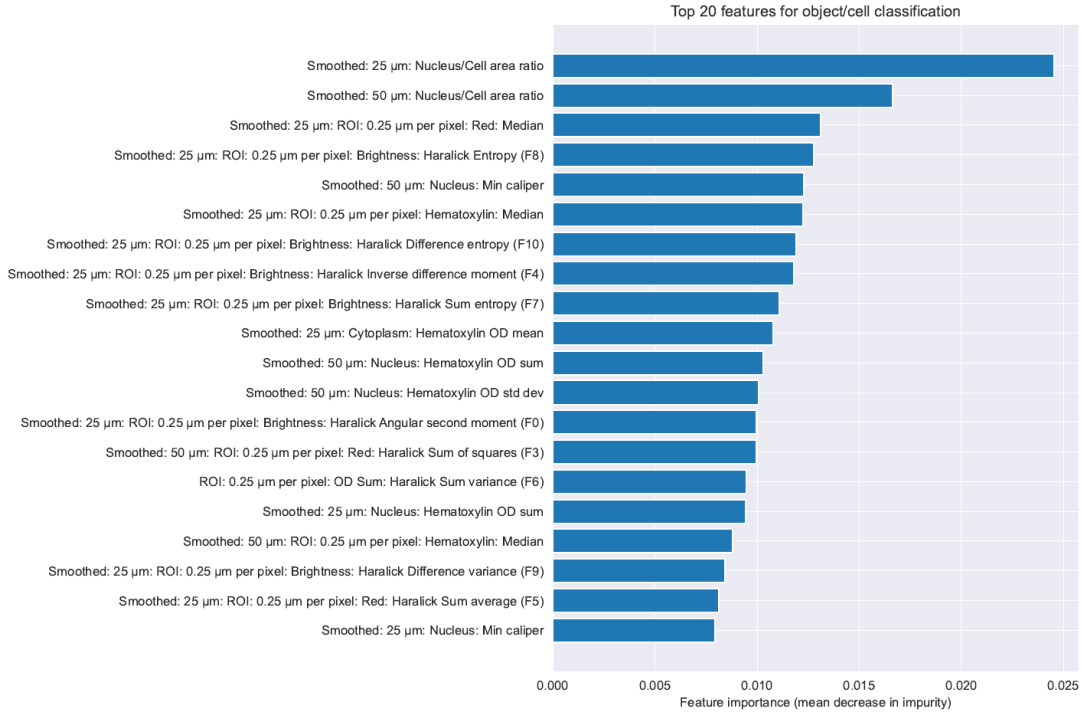

Supplementary Figure 6 Analysis of the top 20 features for object/cell classification using the Random Forest classifier's Gini-based metric (mean decrease in impurity)

Supplementary Figure 7.

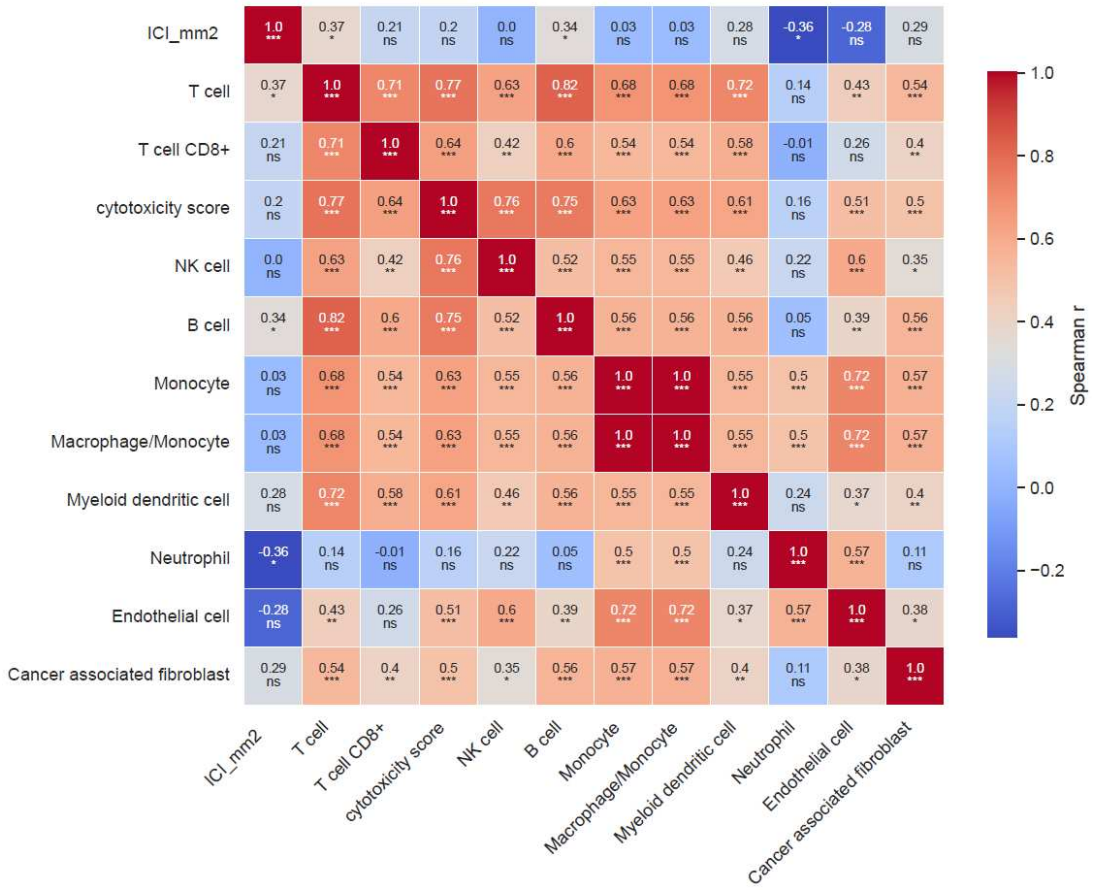

Supplementary Figure 7 Correlation matrix assessing the correlation of the ICI with immune cell signatures based on the RNAseq cohort

Supplementary Figure 8.

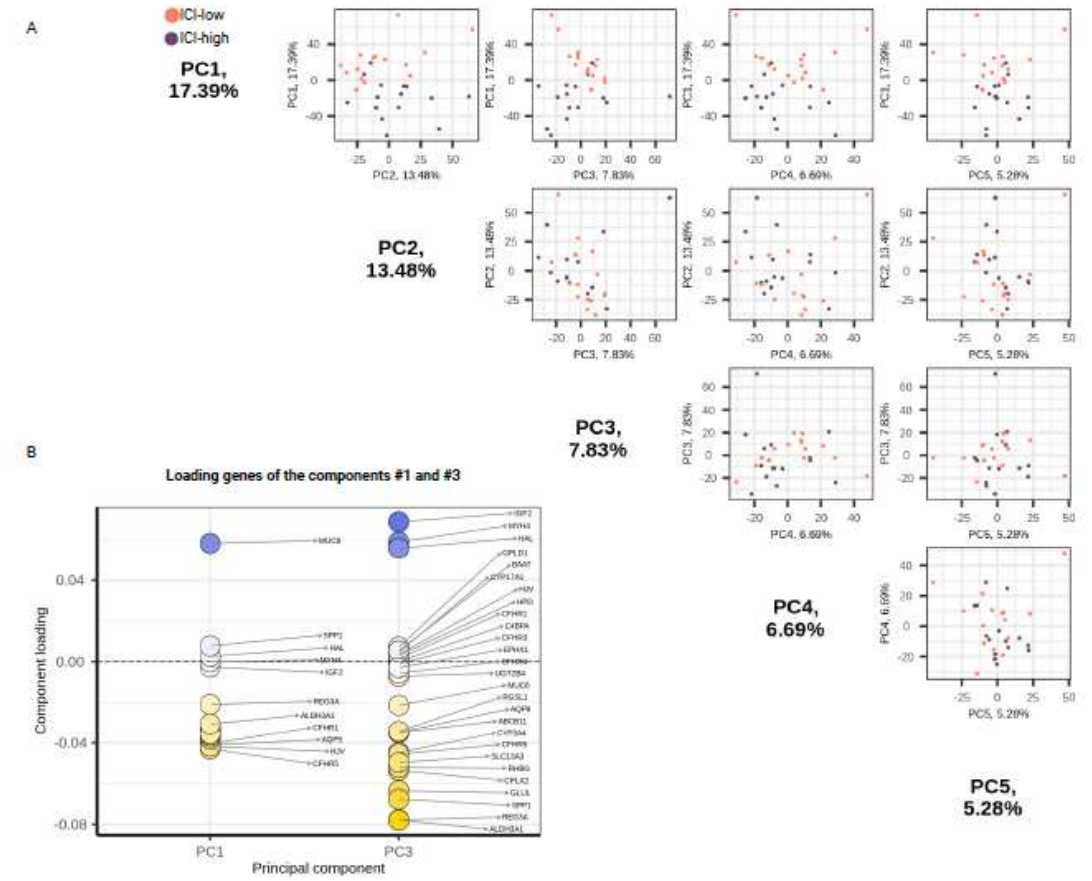

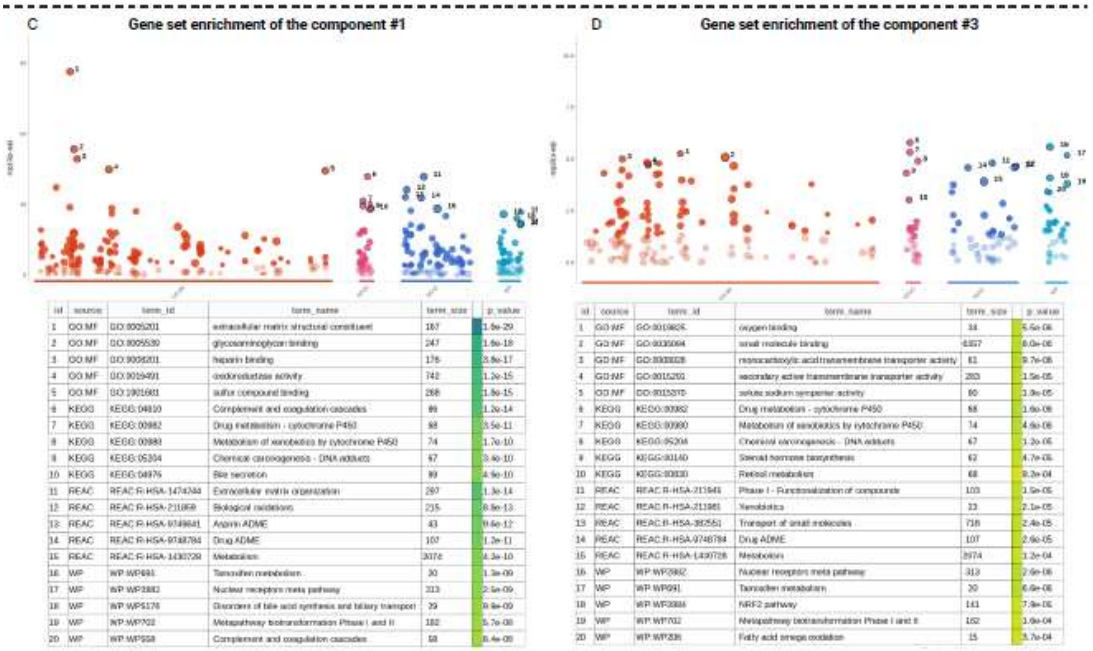

id	source	term_id	term_name	term_size	p_value
1	GO:MF	GO:0005201	extracellular matrix structural constituent	187	1.6e-20
2	GO:MF	GO:0005539	glycosaminoglycan binding	247	1.6e-18
3	GO:MF	GO:0008201	heparin binding	176	3.8e-17
4	GO:MF	GO:0016491	oxidoreductase activity	742	1.2e-15
5	GO:MF	GO:1901681	sulfur compound binding	268	1.6e-15
6	KEGG	KEGG:04610	Complement and coagulation cascades	69	1.2e-14
7	KEGG	KEGG:00982	Drug metabolism - cytochrome P450	68	3.5e-11
8	KEGG	KEGG:00980	Metabolism of xenobiotics by cytochrome P450	74	1.7e-10
9	KEGG	KEGG:05204	Chemical carcinogenesis - DNA adducts	67	3.4e-10
10	KEGG	KEGG:04976	Bile secretion	89	4.9e-10
11	REAC	REAC:R-HSA-1474244	Extracellular matrix organization	297	1.3e-14
12	REAC	REAC:R-HSA-211859	Biological oxidations	215	8.8e-13
13	REAC	REAC:R-HSA-9748641	Aspirin ADME	43	9.6e-12
14	REAC	REAC:R-HSA-9748784	Drug ADME	107	1.2e-11
15	REAC	REAC:R-HSA-1430728	Metabolism	3074	4.3e-10
16	WP	WP:WP691	Tamoxifen metabolism	30	1.3e-09
17	WP	WP:WP3883	Nuclear receptors meta pathway	313	2.5e-09
18	WP	WP:WP5176	Disorders of bile acid synthesis and biliary transport	29	9.8e-09
19	WP	WP:WP702	Metapathway biotransformation Phase I and II	182	5.7e-08
20	WP	WP:WP558	Complement and coagulation cascades	58	8.4e-08

id	source	term_id	term_name	term_size	p_value
1	GO:MF	GO:0019825	oxygen binding	34	6.6e-06
2	GO:MF	GO:0036094	small molecule binding	4357	8.0e-06
3	GO:MF	GO:0008028	monocarboxylic acid transmembrane transporter activity	61	9.7e-06
4	GO:MF	GO:0015291	secondary active transmembrane transporter activity	203	1.5e-05
5	GO:MF	GO:0015370	solute:sodium symporter activity	80	3.9e-05
6	KEGG	KEGG:00982	Drug metabolism - cytochrome P450	68	1.6e-08
7	KEGG	KEGG:00980	Metabolism of xenobiotics by cytochrome P450	74	4.6e-08
8	KEGG	KEGG:05204	Chemical carcinogenesis - DNA adducts	67	1.2e-06
9	KEGG	KEGG:00140	Steroid hormone biosynthesis	62	4.7e-06
10	KEGG	KEGG:00830	Retinol metabolism	68	8.2e-04
11	REAC	REAC:R-HSA-211945	Phase I - Functionalization of compounds	103	1.5e-05
12	REAC	REAC:R-HSA-211981	Xenobiotics	33	2.1e-05
13	REAC	REAC:R-HSA-382551	Transport of small molecules	718	2.4e-05
14	REAC	REAC:R-HSA-9748784	Drug ADME	107	2.6e-05
15	REAC	REAC:R-HSA-1430728	Metabolism	3974	1.2e-04
16	WP	WP:WP3882	Nuclear receptors meta pathway	313	2.6e-06
17	WP	WP:WP691	Tamoxifen metabolism	30	6.6e-06
18	WP	WP:WP3884	NRF2 pathway	141	7.9e-05
19	WP	WP:WP702	Metapathway biotransformation Phase I and II	182	1.9e-04
20	WP	WP:WP206	Fatty acid omega oxidation	15	3.7e-04

Supplementary Figure 8. Analysis of the principal components driving transcriptomic diversity in ICI-high and ICI-low. (A) Combinations of the first five principal components. Although component #3 (PC3) contributed less variance than PC2, it allowed better separation of ICI-high patients. (B) Loading plots demonstrate the genes contributing to PC1 and PC3 the most. Blue color indicates a positive score, and yellow color indicates a negative. (C) Gene set analysis of 200 genes with the strongest positive or negative score in PC1. (D) Gene set analysis of 200 genes with the strongest positive or negative score in PC3. In both cases, only significant gene sets are shown, and the highest ranked gene sets are shown in greater detail. A hypergeometric test was used for gene set enrichment.

Supplementary Figure 9.

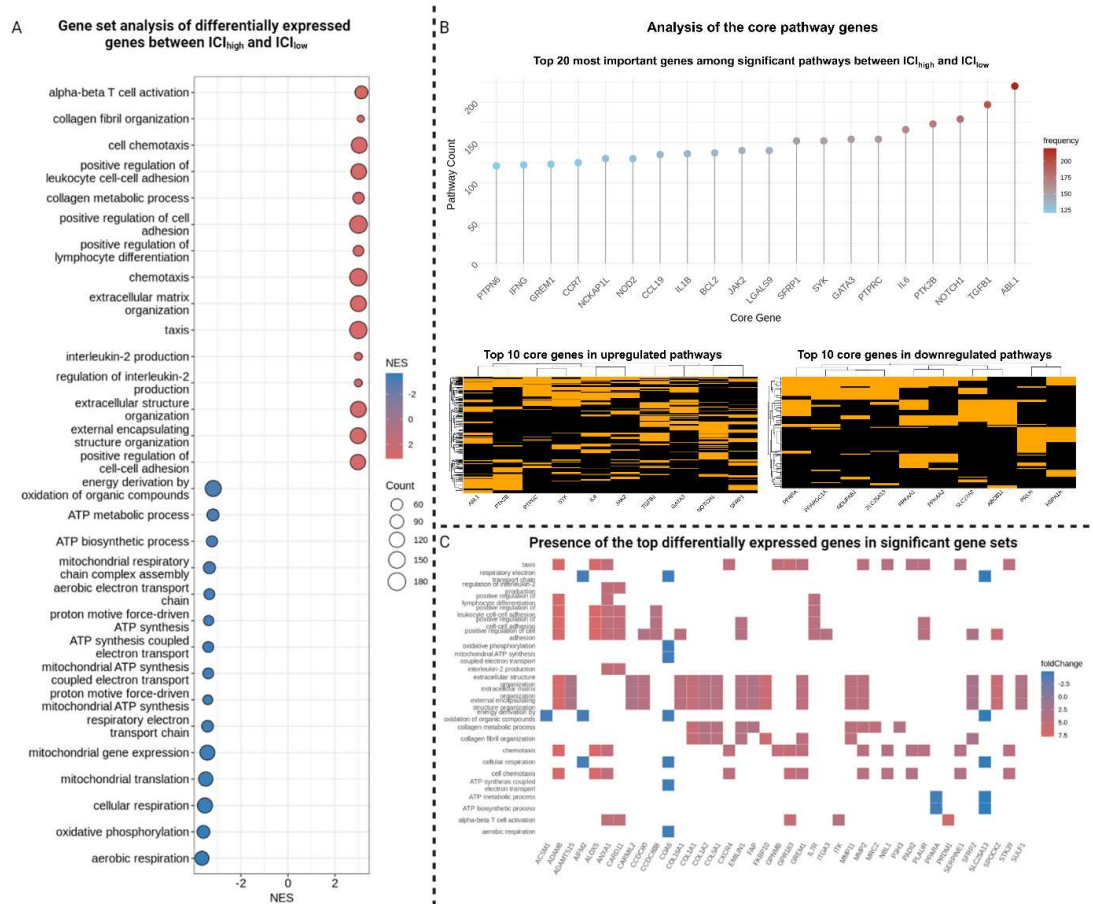

Supplementary Figure 9. Gene set analysis (GO:BP) of differentially expressed genes between ICI-high and ICI-low. (A) Normalized enrichment score (NES, x-axis) indicates the direction of regulation in an inversed way for both groups: negative NES suggests that a pathway is upregulated in ICI-low, while positive NES indicates upregulation in ICI-high. The dot size corresponds to a larger overlap size for a gene set. Only 20 gene sets with the highest and lowest NES are displayed. Gene ranking was performed based on their log2 fold change and significance. (B) Network representing gene overlaps between the gene sets from panel A. Colour reflects the direction of regulation (red = upregulated gene, blue = downregulated gene). (C) Overlap between differentially expressed genes between ICI-high and ICI-low and prioritized gene sets.

Supplementary Figure 10.

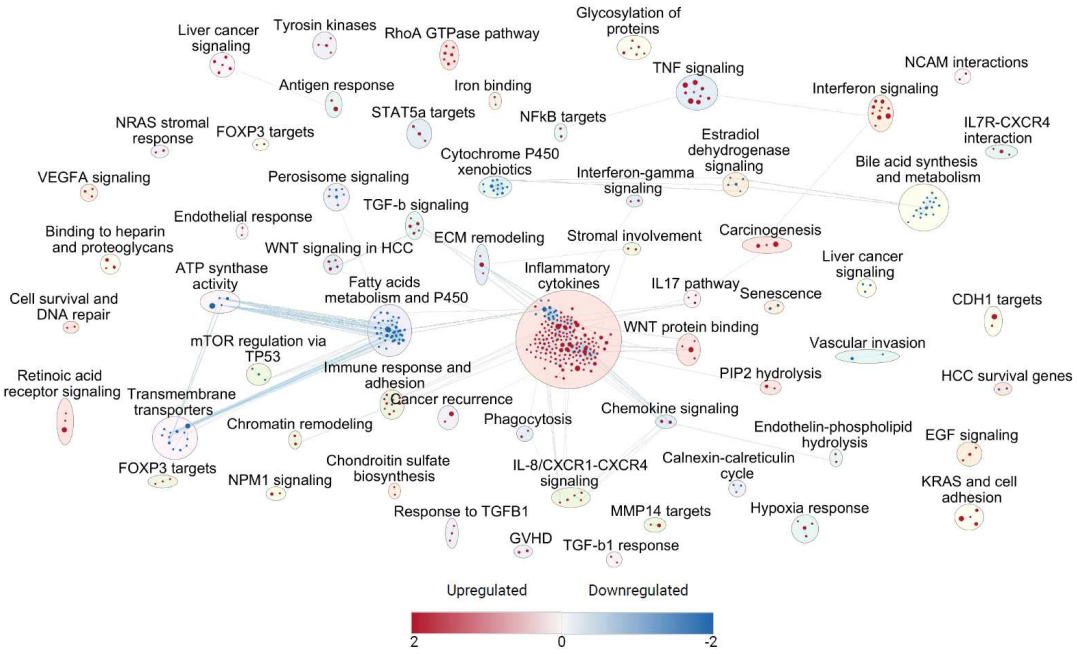

Supplementary Figure 10. **Network of dysregulated pathways between ICI-high and ICI-low**. Each node represents one pathway. Node colour indicates regulation in ICI-high compared to ICI-low: red corresponds to upregulation, and blue – to downregulation. Node size is increased with a higher number of genes in a pathway. Network edges connecting pathways represent overlapping genes, and edge size corresponds to overlap size. Pathways with significant overlaps are clustered together, and the molecular function of each cluster is provided.

Supplementary Figure 11.

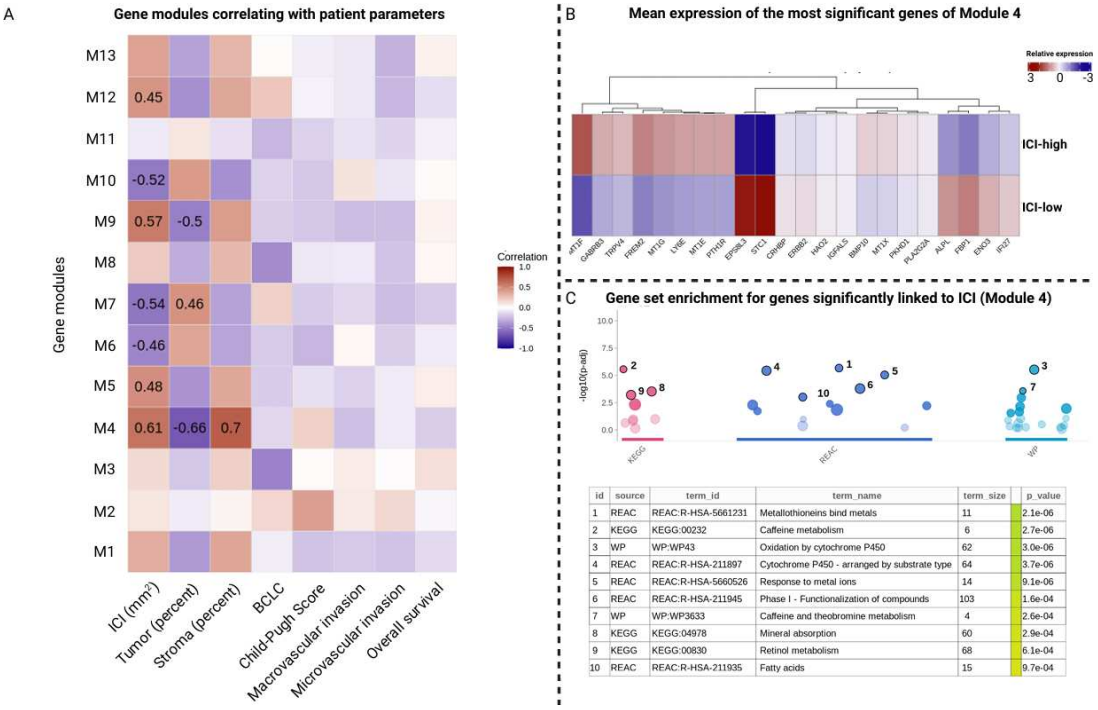

id	source	term_id	term_name	term_size	p_value
1	REAC	REAC:R-HSA-5661231	Metallothioneins bind metals	11	2.1e-06
2	KEGG	KEGG:00232	Caffeine metabolism	6	2.7e-06
3	WP	WP:WP43	Oxidation by cytochrome P450	62	3.0e-06
4	REAC	REAC:R-HSA-211897	Cytochrome P450 - arranged by substrate type	64	3.7e-06
5	REAC	REAC:R-HSA-5660526	Response to metal ions	14	9.1e-06
6	REAC	REAC:R-HSA-211945	Phase I - Functionalization of compounds	103	1.6e-04
7	WP	WP:WP3633	Caffeine and theobromine metabolism	4	2.6e-04
8	KEGG	KEGG:04978	Mineral absorption	60	2.9e-04
9	KEGG	KEGG:00830	Retinol metabolism	68	6.1e-04
10	REAC	REAC:R-HSA-211935	Fatty acids	15	9.7e-04

Supplementary Figure 11. Gene modules linked to the dynamics of patient readouts. (A) Gene co-expression analysis identified gene modules (y-axis) co-expressing with changes in ICI and other confounders (x-axis). The colour indicates the direction of correlation, and *p*-values are provided for modules with significant correlation. Only significant ($p < 0.05$) correlations are displayed with their coefficient. (B) Mean expression of top-ranked genes, included in module 4 (M4 on panel A), linked to ICI dynamics. (C) Gene set analysis of genes significantly linked to ICI abundance changes.